



HAL
open science

First principle investigation of the influence of sulfur vacancies on thermoelectric properties of single layered MoS₂

Ch. Adessi, S. Pecorario, S. Thébaud, G. Bouzerar

► **To cite this version:**

Ch. Adessi, S. Pecorario, S. Thébaud, G. Bouzerar. First principle investigation of the influence of sulfur vacancies on thermoelectric properties of single layered MoS₂. *Physical Chemistry Chemical Physics*, 2020, 22 (26), pp.15048-15057. 10.1039/D0CP01193B . hal-03011492

HAL Id: hal-03011492

<https://hal.science/hal-03011492v1>

Submitted on 27 Nov 2020


HAL is a multi-disciplinary open access archive for the deposit and dissemination of scientific research documents, whether they are published or not. The documents may come from teaching and research institutions in France or abroad, or from public or private research centers.

L'archive ouverte pluridisciplinaire **HAL**, est destinée au dépôt et à la diffusion de documents scientifiques de niveau recherche, publiés ou non, émanant des établissements d'enseignement et de recherche français ou étrangers, des laboratoires publics ou privés.



Cite this: *Phys. Chem. Chem. Phys.*, 2020, 22, 15048

First principle investigation of the influence of sulfur vacancies on thermoelectric properties of single layered MoS₂

Ch. Adessi, * S. Pecorario, S. Thébaud and G. Bouzerar

Thermoelectric properties of single layered transition metal dichalcogenide MoS₂ are investigated on the basis of *ab initio* calculations combined with Landauer formalism. The focus is made on sulfur vacancy defects that are experimentally observed to be largely present in materials especially in exfoliated two dimensional MoS₂ compounds. The impact of these defects on phonon and electron transport properties is investigated here using a realistic description of their natural disordering. It is observed that phonons tend to localize around defects which induce a drastic reduction in thermal conductivity. For p type doping the figure of merit is almost insensitive to the defects while for n type doping the figure of merit rapidly tends to be zero for the increasing length of the system. These features are linked with a larger scattering of the electrons in the conduction band than that of holes in the valence band.

Received 2nd March 2020,
Accepted 4th June 2020

DOI: 10.1039/d0cp01193b

rsc.li/pccp

1 Introduction

The unique electronic,^{1–7} optoelectronic^{8,9} and thermal properties¹⁰ of two-dimensional (2D) van der Waals layered transition metal dichalcogenides such as MoS₂ have led to a keen interest in this material over the last decade. Moreover, 2D transition metal dichalcogenides have emerged as promising compounds for energy¹¹ applications such as energy generation or conversion. Notably, MoS₂ has recently been investigated for prospects in thermoelectricity on both the theoretical^{12–17} and experimental side.^{7,18–20}

The thermoelectric performance of a material is characterized by the dimensionless figure of merit zT :

$$zT = \frac{\sigma \cdot S^2}{\kappa} T, \quad (1)$$

where σ is the electrical conductivity, S is the Seebeck coefficient, κ is the thermal conductivity and T is the temperature. The electrical properties *i.e.* σ and S are usually gathered within the power factor (PF) that reads as $\sigma \cdot S^2$. A good thermoelectric material should thus have both a low κ value and a high PF. In contrast to graphene, the thermal conductivity of MoS₂ is rather low, ranging from 13.3 W m⁻¹ K⁻¹²¹ for the suspended monolayer to 84 W m⁻¹ K⁻¹.²² Note that the κ measurement in this 2D material is very challenging and there is a large dispersion of experimental values, see also ref. 23–25 for instance. In

addition, the PF for pristine MoS₂ may be as high as $2.8 \times 10^4 \mu\text{W K}^{-2} \text{m}^{-1}$.¹⁶

However, depending on the synthesis technique, exfoliated 2D materials may contain a high density of defects. In MoS₂ the defect considered as the most prevalent is sulfur vacancies.^{26,27} Actually, the defect concentration on freshly exfoliated MoS₂ is observed to be as large as 8%.²⁸ This obviously raises the question of the implication of these defects on the physical properties of MoS₂ that is not yet well understood from both the experimental and theoretical point of view. For instance, it has a high impact on the performance of field effect transistors²⁹ and several attempts have been made to tune the physical properties through defect engineering.^{30–32} Regarding the thermal properties, non-equilibrium molecular dynamics calculations have shown a remarkable suppression of the thermal conductivity by point defects in MoS₂ nanoribbons.³³ Such defects induce the localization of phonon modes and a reduction of thermal conductivity due to an enhancement in Umklapp scattering.^{34,35} Furthermore, first principle studies have pointed out that the zT may be as high as 6.24 for MoS₂ with S defects at room temperature.³⁶ The understanding of the interplay between Umklapp processes and defect scattering is still an open and complex issue that implies a realistic treatment of the disordering and thus of the Anderson localization phenomenon.

In this paper, we address the influence of sulfur vacancies on the thermoelectric properties of single layered hexagonal MoS₂ by means of *ab initio* calculations combined with the Green's function technique and Landauer formalism. We provide an insight into the influence of these defects on the figure of merit zT . The goal is to take into account the natural disordering

Univ Lyon, Université Claude Bernard Lyon 1, CNRS, Institut Lumière Matière, F-69622, Villeurbanne, France. E-mail: christophe.adessi@univ-lyon1.fr



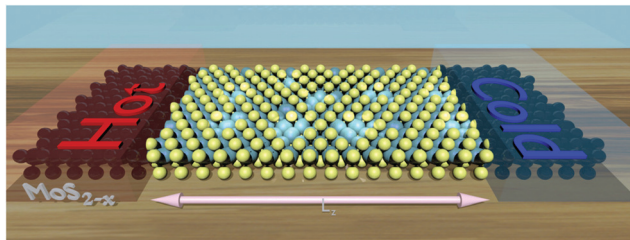


Fig. 1 Artwork of a MoS₂ monolayer within the Landauer formalism. The leads correspond to pristine MoS₂ and the device (between the two leads) corresponds to MoS₂ with randomly located sulfur vacancies.

of sulfur vacancies to investigate the competitive influence of these types of defects on both the power factor and thermal conductivity.

2 Results and discussions

2.1 Theoretical background and methodology

All the calculations are performed using the *ab initio* package SIESTA³⁷ under the generalized gradient approximation of Perdew, Burke & Ernzerhof³⁸ and using Troullier–Martin norm-conserving pseudopotentials.³⁹ The basis used for the calculations corresponds to a double-zeta-polarized basis optimized using the simplex tool of the package. All the atomic structures were optimized up to forces less than 10⁻⁴ eV Å⁻¹. A Monkhorst–pack grid of 10 × 10 × 1 *k*-points has been used for the calculations. For the Hartree potential, a mesh cutoff of 1000 Ry has been applied which corresponds to a typical mesh size of 0.1 Bohr. This very small mesh size is needed in order to obtain the required accuracy for the dynamical matrix.

In the framework of Landauer formalism,^{40–42} the system is divided into two semi-infinite leads and a device (Fig. 1) which includes sulfur vacancies randomly located. The leads correspond to pristine MoS₂ (no vacancy). The thermoelectric properties *i.e.* the Seebeck coefficient, electrical conductance and thermal conductance are computed using the transmission coefficients through the system for the electrons and the phonons. These transmissions are obtained thanks to the Green's functions of the system which are built either from the Hamiltonian (electrons) or the dynamical matrix (phonons). These last operators are obtained from the *ab initio* calculations. This approach is a very efficient way to deal with defects and provides an insight into the effect of sulfur vacancies on the transport properties. The electrical conductance, the Seebeck coefficient and the thermal conductance are defined as follows:

$$G_{e^-} = -\frac{2e^2}{h}L_0(E_F), \quad (2a)$$

$$S = -\frac{1}{k_B T}L_1(E_F)/L_0(E_F), \quad (2b)$$

with,

$$L_n(E_F) = \int_{-\infty}^{+\infty} (E - E_F)^n T_{e^-}(E) \left(\frac{\partial f_{FD}}{\partial E} \right) dE, \quad (2c)$$

$$G_{ph} = -\frac{k_B^2 T}{h} \int_0^{+\infty} \left(\frac{\hbar\omega}{k_B T} \right)^2 T_{ph}(\omega) \left(\frac{\partial f_{BE}}{\partial \omega} \right) d\omega. \quad (2d)$$

In these equations, *e* is the electron charge, \hbar is the reduced Planck constant, *k_B* is the Boltzmann constant, *T* is the temperature, *E_F* is the Fermi energy of the system, *f_{FD}*(*E*) is the Fermi–Dirac distribution and *f_{BE}*(*ω*) is the Bose–Einstein distribution. *T_{e⁻}*(*E*) and *T_{ph}*(*ω*) are, respectively, the electron and phonon transmissions. The equation which defines the phonon thermal conductance involves the derivative of the Bose–Einstein distribution. This derivative (depicted in Fig. 2) figures the respective weight of each conduction channel in conductance. The electronic contribution to the thermal conductance can be defined in a similar way (see ref. 43). However, this contribution is negligible when compared to the lattice contribution as pointed out in ref. 44 and 45. At least 99% of the heat conduction happens through the lattice at room temperature. This behavior is attributed to the small density of states near the Fermi level.

On the basis of the Landauer–Büttiker formalism, the transmission reads:⁴¹

$$T = \text{tr}[\Gamma_L G^r \Gamma_R G^a], \quad (3)$$

where *G^{r(a)}* is the retarded (advanced) Green's function and *Γ_{L(R)}* is the coupling between the left (right) lead and the device as illustrated in Fig. 1. The main advantages of this formalism are to allow to deal with disordered systems and to fully include the quantum backscattering processes. More details on Green's functions formalism may be found in ref. 41, 42 and 46.

2.2 Phonon transport with a single sulfur vacancy

In Fig. 2, the behavior of MoS₂ with a single sulfur vacancy is presented either under periodic boundary conditions or isolated using Landauer formalism. These basic models are intended to pinpoint the effects associated with a defect and to facilitate the interpretation of the more realistic results presented hereafter when defects are randomly located. On top of this figure is pictured the normalized differential occupancy of the Bose–Einstein distribution defined as:

$$N_{\text{diff. occ.}} = \left(\frac{\hbar\omega}{k_B T} \right)^2 \left(\frac{\partial f_{BE}}{\partial \omega} \right). \quad (4)$$

This quantity is involved in the integral (*cf.* eqn (2d)) defining the thermal conductance and characterizes the occupancy of the conduction channels. Notably, at low temperature (50 K) only the low frequency acoustic modes are involved in the transport. Conversely, at room and higher temperatures, all the acoustic modes are involved along with the optical ones. This is consistent with the estimated average acoustic Debye temperature in MoS₂ that is of the order of 260 K (see also ref. 47).

One issue of concern is the localization of the phonon modes induced by the vacancy. This effect can clearly be pointed out by considering the inverse participation ratio (IPR) that reads:

$$\text{IPR} = \sum_{n=1}^N a_n^4 / \left(\sum_{n=1}^N a_n^2 \right)^2, \quad (5)$$



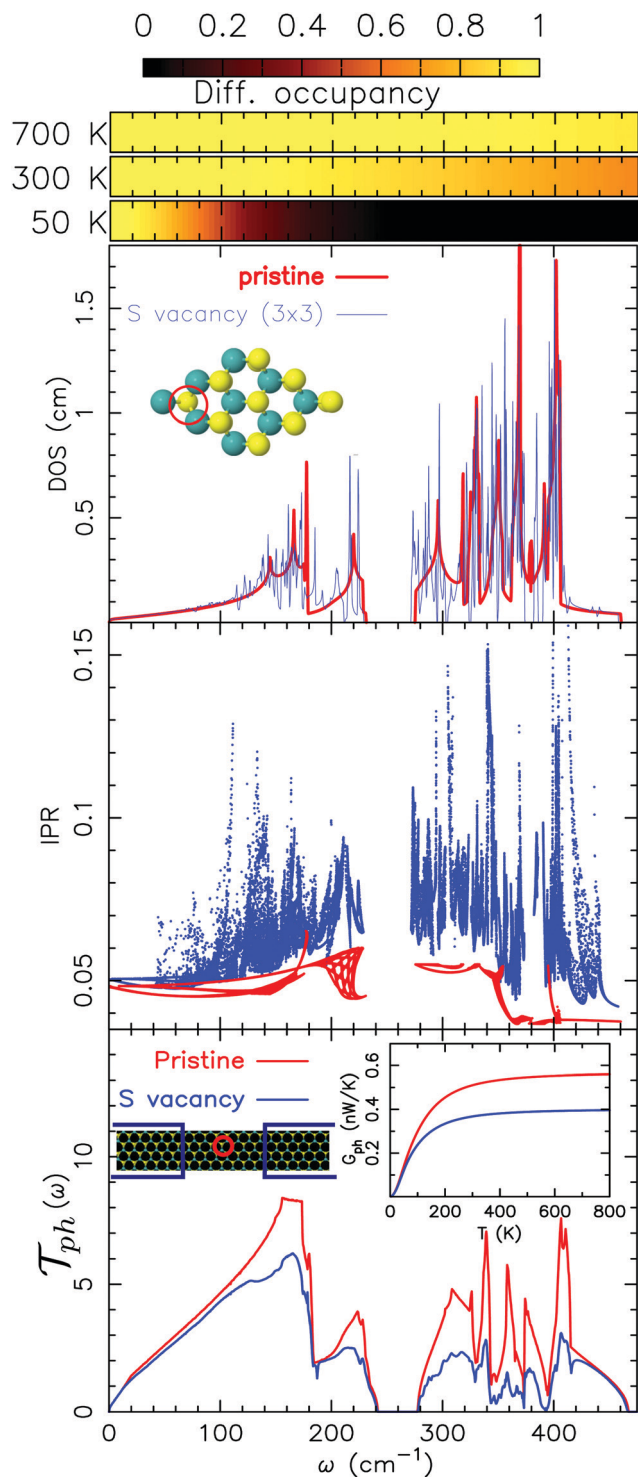


Fig. 2 From top to bottom: Normalized differential occupancy of the Bose–Einstein distribution (as defined in eqn (4)), phonon density of states for a 3×3 cell either for pristine MoS₂ or with a sulfur vacancy, the inverse participation ratio (as defined in eqn (5)) and phonon transmission for pristine MoS₂ and a device with a single sulfur vacancy. All of them are given as functions of the energy of the phonon modes.

where a_n is the n -th component of the eigenvector of a given phonon mode. For a completely delocalized or extended mode, the IPR is equal to $1/N$ (with N being the degree of freedom) and

on the other hand, it is equal to 1 for a fully localized mode on a single site. When compared to the pristine case, the IPR with an S vacancy exhibits a clear localization tendency which is more pronounced for the optical modes (for frequencies higher than 250 cm^{-1}). This localization also has an impact on the density of states (DOS) for which sharp peaks linked with these localized modes can be observed mainly for the optical branches.

The role of an isolated vacancy in the transport properties is actually linked with the previous remark. When we compare the transmission between the pristine case and that of the one with a sulfur vacancy, it is mainly the in-plane optical modes that are affected by the defect. More remarkably, the in plane optical modes (in the frequency range from 250 cm^{-1} to 420 cm^{-1} , see Fig. 7) are the most scattered modes in contrast to the ZO modes (above 420 cm^{-1}) that are almost unaffected. Despite the rather high frequency of LO–TO modes, this has a significant influence on the thermal conductance (see the inset of Fig. 2). Indeed, the thermal conductance defined by means of the phonon transmission in eqn (2d) involves the derivative of the Bose–Einstein distribution. This derivative is represented on top of Fig. 2. Given that the spectrum range of MoS₂ is rather narrow (compared to graphene,⁴⁸ for instance), almost all the conduction modes (acoustic and optical) are involved in the transport at room temperature. The direct consequence, when mixed with the scattering of the optical modes, is a reduction in conductance by almost one-third at room temperature compared to that of the pristine case.

2.3 Electronic transport with a single sulfur vacancy

As mentioned in the theoretical section, we need to deal with both the thermal and electronic properties to estimate the zT . Thus, in this section we address the influence of a single sulfur vacancy on the electronic transport properties of MoS₂. The main aim is to provide an insight into the influence of such defect.

In Fig. 3, the fundamental difference between a calculation done on a periodic system and a disordered one is pointed out. On top of this figure, the electronic density of states for a 3×3 periodic cell with a sulfur vacancy is given. This vacancy induces specific bands within the band gap of the material. These bands are less dispersed and one is fully occupied.⁴⁹ However, the occurrence of these bands is closely related to their periodicity. This is illustrated in the transmission. We have either considered a system with a sulfur vacancy repeated periodically (each unit cell corresponds to $(\text{MoS}_{1.958})_{24}$) or a device (with a length L_z of 13 nm) on which the vacancies are randomly distributed.† Note that both of them have the same vacancy density. For the periodic case the bands induced by the vacancy lead to well defined conduction channels. However, periodic defects are not realistic and it can clearly be seen that for the disordered system these channels are almost fully suppressed (note the logarithmic scale). This means that it is only the native bands of the material (not the ones induced by

† For the disordered system, we have performed several calculations with different vacancy distributions; all of them lead to similar results.



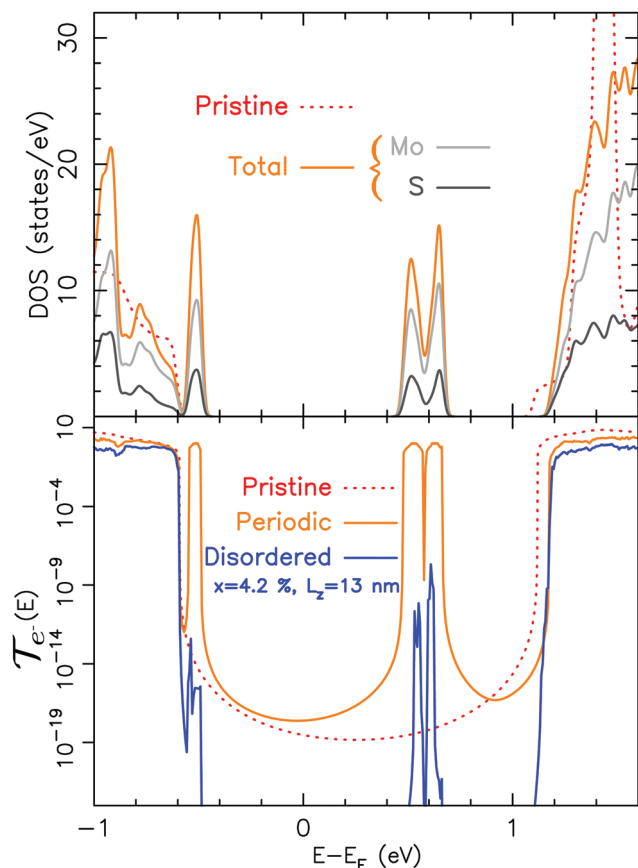


Fig. 3 From top to bottom: Electronic density of states for a 3×3 MoS₂ cell with a sulfur vacancy and electronic transmission for a device with sulfur vacancies either periodic or randomly located (disordered). Both of them are represented as functions of energy (centered at the Fermi level). For the transmission, x is the vacancy density defined as MoS_{2-x}.

the vacancy) which can play a role in the transport. This is compatible with the experimental observations of a variable range hopping^{50,51} and also with STM measurements.⁵²

Fig. 4 depicts the electrical conductance, the Seebeck coefficient and the PF (at 300 K and 700 K) either in pristine MoS₂ or in a compound with a single sulfur vacancy. Here, we have considered a rigid band shift model, wherein the position of the Fermi level is shifted rigidly either toward the valence band or towards the conduction band to mimic hole or electron doping, respectively. The dashed lines correspond to the positions of the Fermi level for which the PF is maximum. In what follows, zT will be estimated for the electron/hole density that maximizes the PF. Let us now focus on the energy range that is relevant for the transport properties. Note that only narrow regions close to the top of the valence band and to the bottom of the conduction band are relevant to the transport. These energy windows result from the derivative of Fermi distribution involved in the equations that define the Seebeck coefficient and the electrical conductance (see eqn (2b) and (2a)). This is illustrated in the inset of Fig. 4 representing the transmission. The shaded green regions represent the energy windows around the Fermi level that have a significant weight for the

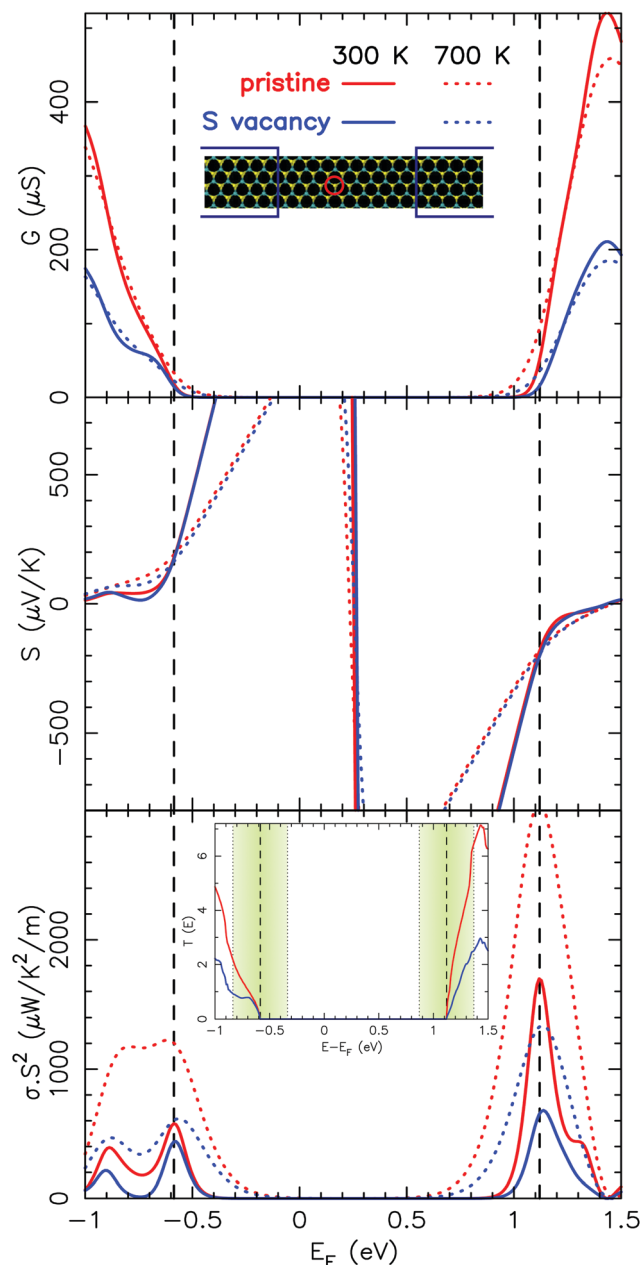


Fig. 4 From top to bottom: Electrical conductance, the Seebeck coefficient and the power factor for pristine MoS₂ and MoS₂ with a single sulfur vacancy as functions of the Fermi level at either 300 K or 700 K. The inset of the power factor depicts the corresponding transmission coefficients along with the illustration of the relative weight at 700 K (in shaded green) of the conduction channels in the conductance at the maximum of the power factor either for the valence or the conduction band.

transport at 700 K. Of course, at room temperature, these windows are about two times smaller.

Regarding the valence band, the influence of the sulfur vacancy is significant only at low energy (with respect to the top of the valence band). For this reason, the impact on the maximum of the PF (when compared to the pristine case) is modest at room temperature but clearly noticeable at 700 K. At this temperature, the PF obtained with the defect is 2 times



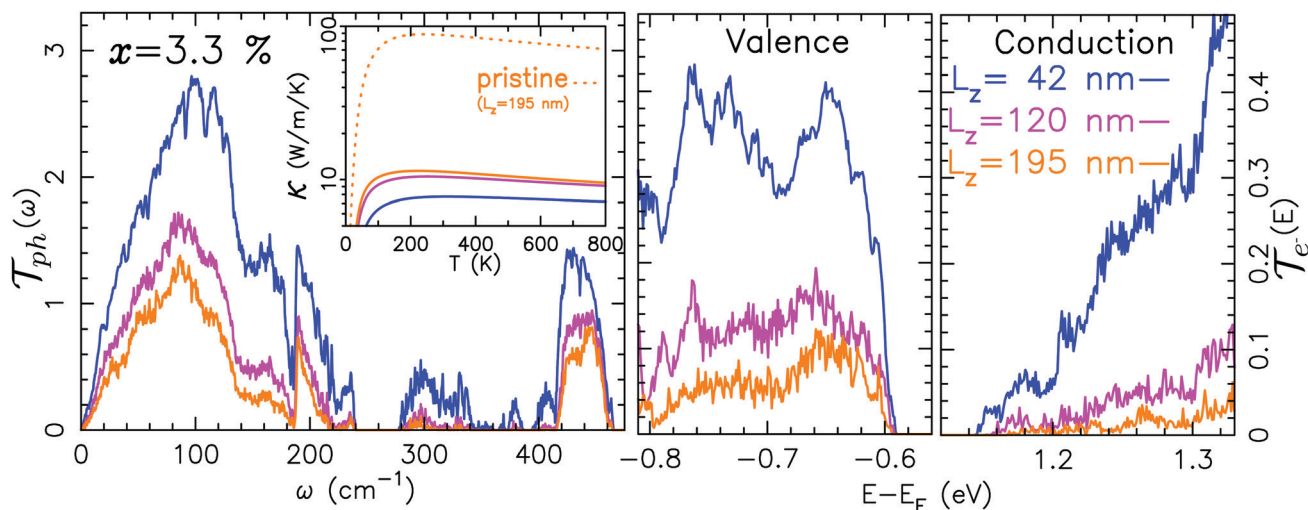


Fig. 5 Transmission coefficient for phonons (left) or electrons (right) as a function of either frequency or energy for a system containing 3.3% of sulfur vacancies and for 3 different lengths. In the inset of the phonon transmission is given the thermal conductivity as a function of temperature for both defective and pristine compounds.

smaller than that of the pristine case. Conversely, the influence of the defect on the conduction band is noticeable until the very bottom of the band. Thus, for n-type doping, the decrease of the PF is much more important and significant whatever the temperature is. As presented hereafter this trend is also observed in disordered systems. One should note that the Seebeck coefficient is almost unaffected by the defect and the observed variations of the PF are mainly due to the variations of the electrical conductance.

To explain the different impact of the sulfur vacancy on the valence and conduction bands, one should keep in mind that the first nearest neighbors of the S vacancy are Mo atoms. In addition, the projected DOS of MoS₂ (see, for instance, ref. 53) consists mainly of Mo d-type contribution for the bottom of the conduction band, and a mix of Mo d-type and S p-type contributions for the top of the valence band. Indeed, the vacancy modifies significantly the onsite potential experienced by the Mo atoms in contrast to its weakest effect on the onsite potential experienced by S atoms.‡ Hence, scattering is expected to be stronger for the states at the bottom conduction band than for those at the top of the valence band.

2.4 Figure of merit in disordered MoS_{2-x}

Let us proceed further and consider now the more realistic case of finite concentration of sulfur vacancies and its effect on the zT . To this end, we have considered systems composed of 2 pristine MoS₂ leads connected to a device where the sulfur vacancies are randomly located with a given vacancy concentration x . In this section, all the results correspond to an average over 10 different compounds with the random distribution of the vacancies. This gives us results with a typical

‡ For the nearest neighbor Mo atoms, the average variation of the on-site potential is 0.42 eV (compared with the pristine case) and it is only 0.13 eV for the nearest S atoms.

standard deviation smaller than the size of the symbols used in the figures. We have considered vacancy densities ranging from 0.8% to 4.2% that correspond to surfacic densities ranging from $9.7 \times 10^{12} \text{ cm}^{-2}$ to $4.9 \times 10^{13} \text{ cm}^{-2}$. Note that these values agree well with the typical densities measured experimentally.²⁷

Fig. 5 depicts the transmission coefficients for both phonons and electrons (the valence and the conduction bands are shown separately). These transmissions are given for the increasing length of the device *i.e.* the region that contains the defects. Regarding the phonon transport, it is the in-plane optical modes that are most affected by the vacancies as previously observed in the single vacancy case. As can be clearly seen, for the increasing length of the system, the in plane optical channels are almost fully suppressed. In contrast, both the acoustic and ZO modes (out of plane optical modes at frequencies above 400 cm^{-1} , see Fig. 7) are weakly affected by the vacancies. The reduction in thermal conductivity§ as seen in the inset of Fig. 5 reflects the suppression of the in-plane optical modes (especially at room and higher temperatures) by multiple scattering on S vacancies. It should be emphasized that here the calculation of the conductivity includes phonon-phonon Umklapp scattering *via* the mode Grüneisen parameters (see, for instance, ref. 54). The details of the procedure are given in Section 4. A more refined study based on the calculations of third order interatomic force constants may be found in ref. 55. However, the device lengths considered here are of the same order of magnitude of the typical mean free path associated with phonon-phonon Umklapp scattering (as shown in Fig. 10). For this reason its effect is less and the associated reduction of the conductivity at high temperature is only noticeable for the longest system size. Nonetheless, the comparison of κ for pristine and defective MoS₂ clearly shows that, for this device

§ Thermal conductivity is defined as: $\kappa = G_{\text{ph}} \times L_z / (L_x L_y)$, where L_z is the length of the device, L_x is the dimension of the MoS₂ layer perpendicular to the transport direction, L_y is the thickness of the layer (typically 6.4 \AA) and G_{ph} is the phonon conductance as defined in eqn (2d).



size, the main mechanism of the reduction of κ is scattering by the defects. This suggests that the length scale on which phonons are scattered by the defects is smaller than the Umklapp one. Furthermore, note the good quantitative agreement for κ between our calculations and experimental values. Indeed, we find, respectively, $90 \text{ W m}^{-1} \text{ K}^{-1}$ for the pristine case and $12 \text{ W m}^{-1} \text{ K}^{-1}$ for the 3.3% defective compound to be compared with the experimental data which range from $13.3 \text{ W m}^{-1} \text{ K}^{-1}$ to $84 \text{ W m}^{-1} \text{ K}^{-1}$.^{21,22} This corroborates our analysis on the competitive influence of Umklapp and defect scattering. The typical length scales that control the transport properties are further discussed in what follows.

Regarding electron transport, the conduction band (n-doping) is impaired the most by the vacancies, especially at the bottom of the band which is the energy spot of interest when computing the power factor. A backscattering is also noticeable for p-doping. However, at the top of the valence band (the region of interest for the PF), the influence of the vacancies is less crucial. As presented hereafter, this difference in behavior between n and p-type doping has a direct repercussion on zT .

The figure of merit is the result of the antagonist effects of the thermal and electron transport properties associated with κ and the PF. If κ is less altered than the PF, the zT will be low and conversely, if κ is more altered than the PF, the zT will be large. Actually, depending on the sulfur vacancy concentration and on the type of doping (n or p), the two situations are encountered. Fig. 6 depicts the figure of merit for n and p-type MoS₂ with different vacancy concentrations. For p-type doping the system is relatively insensitive to defects. At room temperature the zT remains constant as we vary the system length. This means that the combined effects of the vacancies on κ and on the PF compensate each other. It is only at high temperature (700 K) that the PF decreases more rapidly than κ , leading to a reduction in the zT with the system size. This trend originates from the integration window in eqn (2a) and (2b) defining G and S . Its width increases with temperature and at 700 K it includes an area on which the transmission for the valence band is significantly reduced by the defects. However, the zT is nonetheless of the order of 0.5. On the other hand, for n-type doping, the picture is drastically different. The zT decreases very rapidly with the length of the system. At room temperature

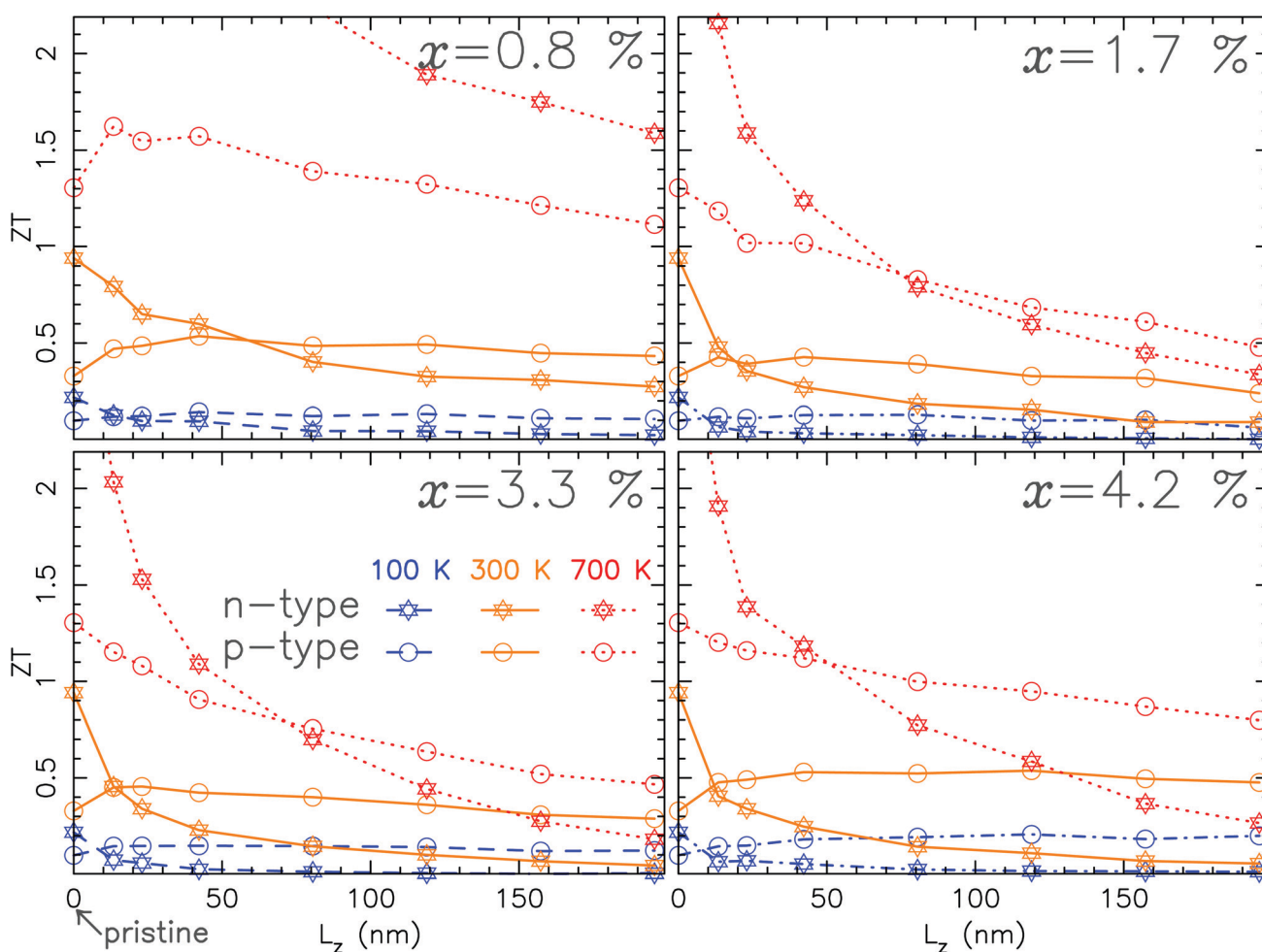


Fig. 6 Figure of merit as a function of the length of the system for 4 different sulfur vacancy concentrations and 3 different temperatures. Note that the values at $L_z = 0$ correspond to the pristine case.



Table 1 Typical length scales for the PF and thermal conductivity obtained from an exponential fit as a function of the system length

	L_{PF} (nm)		L_{κ} (nm)
	n-Type	p-Type	
100 K	31	129	159
300 K	58	107	150
700 K	53	88	146

it drops to almost negligible values especially at large vacancy concentration. It is only at low concentration that the zT has more attractive values. At higher temperature the zT reaches values of the same magnitude than those obtained for p-type doping. However, a rapid decrease of the zT with the length is still observed. This behavior is related to the large influence of the sulfur vacancies on the conduction band, and hence on the PF. For pristine MoS₂, the conduction band is supposed to lead to a larger PF than the valence band. This does not go well with sulfur vacancies which wipe out the conduction channels. Therefore the only way to maintain a significant zT for n-type doping is to have a very low vacancy concentration.

The behavior of the zT portrayed previously is closely related to the decay with the system size of both the PF and thermal conductivity. This behavior is illustrated in Fig. 9 for the PF and a similar behavior is observed for κ (not shown). Indeed, the PF and thermal conductivity follow an exponentially decreasing trend with the length. The characteristic lengths, denoted as L_{PF} for the PF and L_{κ} for κ , are associated with the localization length⁵⁶ of the electron eigenstates (respectively phonon modes). L_{PF} and L_{κ} as functions of temperature are summarized in Table 1. As expected, L_{PF} is significantly larger for p-type than for n-type doping whatever the temperature. In addition, these lengths are typically of the order of 55 nm for n-type doping and 100 nm for p-type doping. Moreover, L_{κ} is always larger than L_{PF} . This is directly reflected in the rapid decrease of the zT with the length of the device reported previously. Note that this decaying length scale is almost insensitive to temperature. As discussed previously, these features are consistent with the fact that the scattering lengths associated with the defects are smaller than those of the Umklapp processes. Let us further discuss the competition between L_{PF} and L_{κ} for p-type doping. At 100 K (and in a few instances at 300 K) the 2 lengths are almost equivalent leading to a zT almost constant with the device size as illustrated in Fig. 6. In contrast, at 700 K, L_{PF} becomes much smaller causing a rapid drop in the zT .

3 Conclusion

In this paper we have addressed, on the basis of *ab initio* calculations and Landauer formalism, the effects of sulfur vacancies on the thermoelectric properties of single layered hexagonal MoS₂. We have investigated both the phonon and electron transport properties of this material by treating the disorder effects realistically. It appears that in plane phonon optical modes are very sensitive to sulfur vacancies and are more likely to be scattered by them. However, the mechanism

which is governing the thermoelectric figure of merit is mostly linked with the PF. For p-type doping the electronic transport properties are less impaired by S vacancies. This leads to a zT almost independent of the length of the system and of the vacancy concentrations. Conversely, for n-type doping, scattering is massive and it leads to a drastic reduction in the zT . These features are related to typical decaying length scales for both the PF and κ revealing that scattering with the vacancies is a dominant mechanism in these disordered systems.

4 Supplementary data

In Fig. 7, the phonon dispersion for 2D MoS₂ is given. The acoustic out of plane mode (ZA) has the typical parabolic shape of a 2D material at the Γ point corresponding to the in plane modes (LA and TA). The optical out of plane modes (denoted as A_1' and A_2'') are well separated from the other modes at the top of the dispersion between 400 and 470 cm^{-1} .

The amplitude of the PF strongly depends on the Fermi level. Indeed, the PF is the product of σ and the square of S which have two opposite trends with the Fermi level. This leads to a bell-shaped function for the PF with a maximum at a given optimal Fermi level (see Fig. 4). The zT , as shown in Fig. 6, is evaluated using the maximum value of the PF. This choice is definitely an open issue as it would result in tuning each vacancy concentration, temperature and length of the system at the optimal Fermi level. In Fig. 8 we have compared the zT (with a vacancy concentration of 4.2%) using either the optimal Fermi level (as in Fig. 6) or a fixed Fermi level close to the top (bottom) of the valence (conduction) band, respectively. For each type of doping, we considered two different values at the Fermi level. These values are in close vicinity of the maximum of the PF obtained for the pristine case (see Fig. 4). As expected, a fixed Fermi level is leading to smaller values of the zT as the

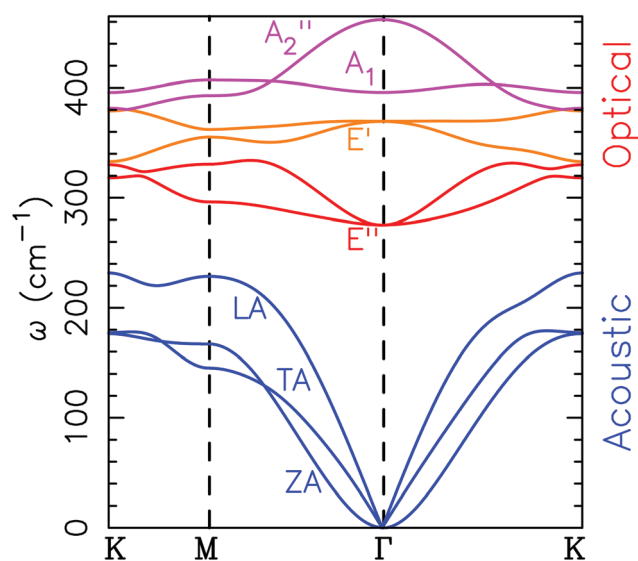


Fig. 7 Phonon dispersion modes for two dimensional MoS₂. A_1' and A_2'' are out of plane optical modes (usually represented as ZO), and E' and E'' are in plane optical modes.



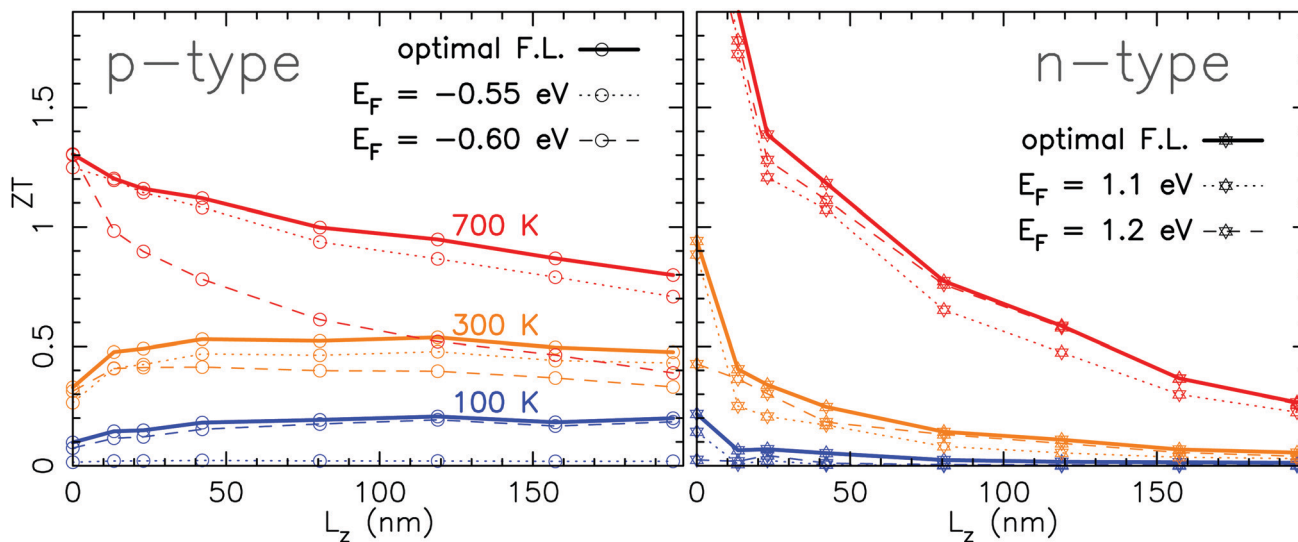


Fig. 8 Figure of merit as a function of the length of the system for a sulfur vacancy concentration of 4.2% and 3 different temperatures. The solid lines correspond to the optimal Fermi level (giving rise to the maximum of the PF and hence of the zT). The dashed and dotted lines correspond to a fixed Fermi level.

PF is not at its maximum. However, the trends pointed out in Section 2.4 for the zT with the length are not affected. For n-type doping the deviation from the optimal case is of the order of 0.2. Indeed, for n-type doping, the optimal Fermi level is almost constant (ranging from 1.14 eV to 1.16 eV) regardless of the length and the temperature of the system. For p-type doping, the optimal Fermi level varies a bit more with the length and mainly with the temperature. This leads to larger deviations of the zT . At 100 K, the optimal Fermi level is -0.61 eV and at 700 K it is -0.51 eV which is much closer to the top of the valence band.

Fig. 9 gives the PF as a function of the length of the system. It is computed using a rigid band shift model. These values correspond to the maximum of the PF (as illustrated in Fig. 4). The electrical conductivity is defined as $\sigma = G/L_y$ where L_y is the thickness of the layer (typically 6.4 Å). Beyond 50 nm, the PF

follows a typically exponentially decreasing trend with a characteristic length L_{PF}^{56} i.e. it follows a decay law of the form $e^{-L_z/L_{PF}}$.

To include the effect of Umklapp scattering, we have made an assumption that the scattering of the phonons by the defects (sulfur vacancies) and the phonon–phonon Umklapp processes are uncorrelated. With this assumption, the phonon transmission coefficient is defined as follow:

$$T(\omega) = \frac{L_x}{2\pi} \int_0^{2\pi/L_x} dq_x \tilde{T}(q_x, \omega) \cdot \frac{\tilde{\lambda}(q_x, \omega)}{L_z + \tilde{\lambda}(q_x, \omega)}, \quad (6)$$

where $\tilde{T}(q_x, \omega)$ is the phonon transmission coefficient which includes scattering by the defects (x is the direction perpendicular to the direction of transport) and $\tilde{\lambda}(q_x, \omega)$ is the mean free path (averaged over q_z) associated with phonon–phonon Umklapp scattering. This integral is obtained using 400 discrete points for q_x . The fraction involving L_z and $\tilde{\lambda}(q_x, \omega)$ in this equation is introduced to have a continuity between the ballistic and the diffusive regime. If $L_z \gg \tilde{\lambda}$ the fraction tends to $\tilde{\lambda}/L_z$ and if $L_z \ll \tilde{\lambda}$ it tends to 1 which corresponds to a ballistic regime for the Umklapp processes. The mean free path per mode is defined using the mode Grüneisen parameter:⁵⁷

$$\begin{aligned} A(\omega_\alpha(\vec{q})) &= v_\alpha(\vec{q}) \cdot \tau_\alpha(\vec{q}) \\ &= v_\alpha(\vec{q}) \cdot \frac{M}{k_B \cdot T} \frac{v_\alpha^2(\vec{q})}{\gamma_\alpha^2(\vec{q})} \cdot \frac{\omega_\alpha^{\max}}{\omega_\alpha^2(\vec{q})}, \end{aligned} \quad (7)$$

where $v_\alpha(\vec{q})$ is the group velocity, $\tau_\alpha(\vec{q})$ is the relaxation time, M is the mass of the unit cell, ω_α^{\max} is the Debye frequency, $\gamma_\alpha(\vec{q})$ is the Grüneisen parameter and $\omega_\alpha(\vec{q})$ is the frequency of the mode α . The Grüneisen parameter for the system with a sulfur vacancy is computed using the post-processing tool phonopy.⁵⁸ In Fig. 10 the group velocity, the phonon lifetime and the mean free path values are shown after computation using eqn (7). The results obtained with a sulfur vacancy correspond to a 3×3 cell.

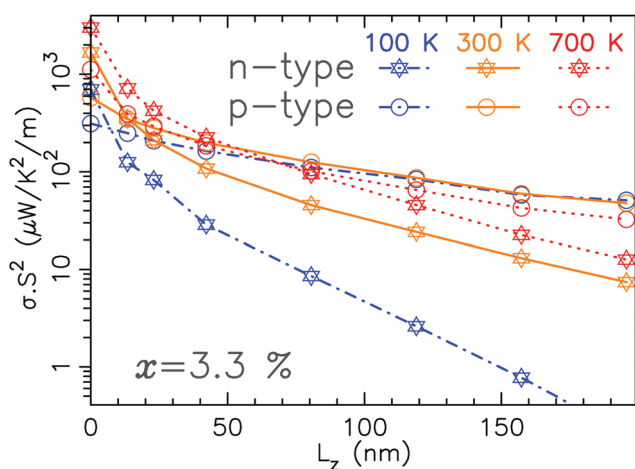


Fig. 9 Power factor for n-type and p-type MoS_{2-x} ($x = 3.3\%$) as a function of the length of the device and for 3 different temperatures.



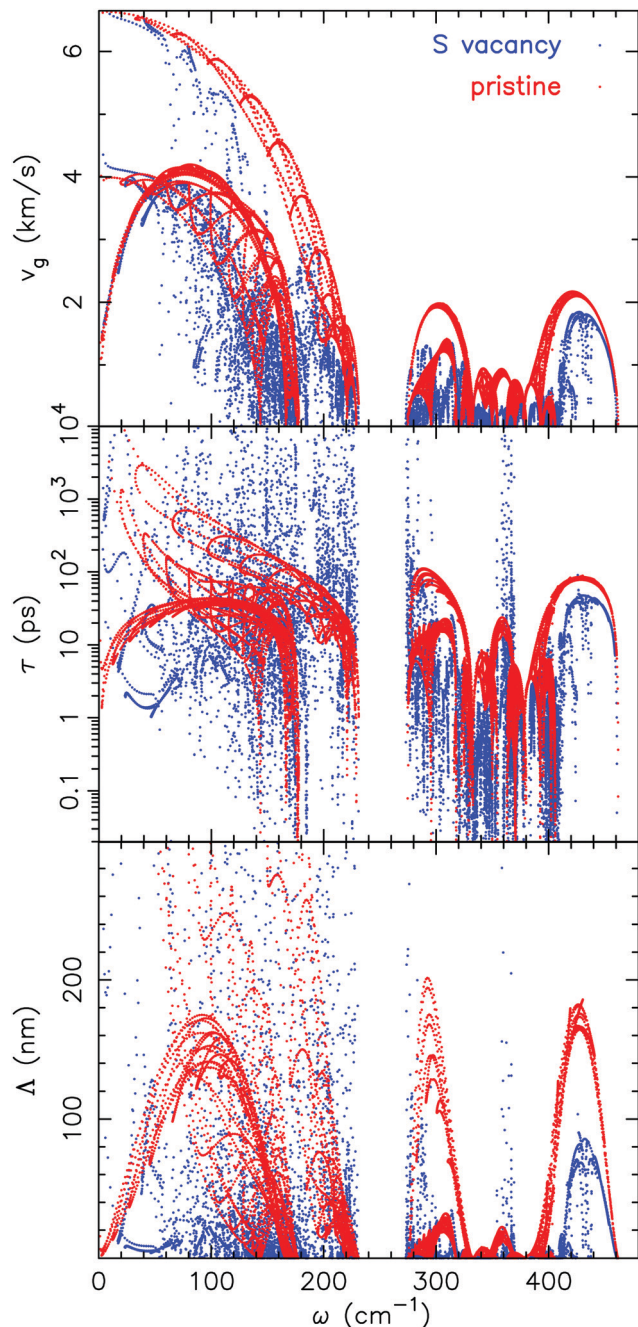


Fig. 10 From top to bottom group velocity, phonon lifetime and the mean free path (as computed in eqn (7)) for either pristine MoS₂ or for a 3 × 3 cell with a sulfur vacancy.

As already pointed out in Section 2.2, the vacancy induces a localization of the phonon modes which leads here to a reduction and to a larger dispersion of the values compared to the pristine case.

To obtain $\tilde{\Lambda}(q_x, \omega)$ as defined in eqn (6), we average $\Lambda(\omega_x(\vec{q}))$ over the reciprocal vector q_z (where z is the direction of transport):

$$\tilde{\Lambda}(q_x, \omega) = \frac{L_z}{2\pi} \sum_x \int_0^{2\pi/L_z} dq_z \Lambda(\omega_x(\vec{q})) \times \Pi\left(\frac{\omega - \omega_x(\vec{q})}{\Delta}\right), \quad (8)$$

where Π is a normalized rectangular function of width Δ (taken as equal to the frequency step used to compute the transmission).

Conflicts of interest

There are no conflicts to declare.

Notes and references

- 1 K. F. Mak, C. Lee, J. Hone, J. Shan and T. F. Heinz, *Phys. Rev. Lett.*, 2010, **105**, 136805.
- 2 E. S. Kadantsev and P. Hawrylak, *Solid State Commun.*, 2012, **152**, 909–913.
- 3 B. Radisavljevic, A. Radenovic, J. Brivio, V. Giacometti and A. Kis, *Nat. Nanotechnol.*, 2011, **6**, 147–150.
- 4 D. Lembke and A. Kis, *ACS Nano*, 2012, **6**, 10070–10075.
- 5 S. Das, H.-Y. Chen, A. V. Penumatcha and J. Appenzeller, *Nano Lett.*, 2012, **13**, 100–105.
- 6 M. Buscema, M. Barkelid, V. Zwiller, H. S. J. van der Zant, G. A. Steele and A. Castellanos-Gomez, *Nano Lett.*, 2013, **13**, 358–363.
- 7 J. Wu, H. Schmidt, K. K. Amara, X. Xu, G. Eda and B. Özyilmaz, *Nano Lett.*, 2014, **14**, 2730–2734.
- 8 H. S. Lee, S.-W. Min, Y.-G. Chang, M. K. Park, T. Nam, H. Kim, J. H. Kim, S. Ryu and S. Im, *Nano Lett.*, 2012, **12**, 3695–3700.
- 9 Z. Yin, H. Li, H. Li, L. Jiang, Y. Shi, Y. Sun, G. Lu, Q. Zhang, X. Chen and H. Zhang, *ACS Nano*, 2012, **6**, 74–80.
- 10 E. Yalon, C. J. McClellan, K. K. H. Smithe, M. Muñásoz Rojo, R. L. Xu, S. V. Suryavanshi, A. J. Gabourie, C. M. Neumann, F. Xiong, A. B. Farimani and E. Pop, *Nano Lett.*, 2017, **17**, 3429–3433.
- 11 N. Choudhary, M. A. Islam, J. H. Kim, T.-J. Ko, A. Schropp, L. Hurtado, D. Weitzman, L. Zhai and Y. Jung, *Nano Today*, 2018, **19**, 16–40.
- 12 Z. Jin, Q. Liao, H. Fang, Z. Liu, W. Liu, Z. Ding, T. Luo and N. Yang, *Nat. Sci. Rep.*, 2015, **5**, 18342.
- 13 W. Huang, H. Da and G. Liang, Thermoelectric performance of MX₂ (M = Mo, W; X = S, Se) monolayers, *J. Appl. Phys.*, 2013, **113**, 104304.
- 14 W. Huang, X. Luo, C. K. Gan, S. Y. Quek and G. Liang, Theoretical study of thermoelectric properties of few-layer MoS₂ and WSe₂, *Phys. Chem. Chem. Phys.*, 2014, **16**, 10866–10874.
- 15 D. D. Fan, H. J. Liu, L. Cheng, P. H. Jiang, J. Shi and X. F. Tang, *Appl. Phys. Lett.*, 2014, **105**, 133113.
- 16 H. Babaei, J. M. Khodadadi and S. Sinha, *Appl. Phys. Lett.*, 2014, **105**, 193901.
- 17 R.-N. Wang, G.-Y. Dong, S.-F. Wang, G.-S. Fua and J.-L. Wang, *Phys. Chem. Chem. Phys.*, 2017, **19**, 5797–5805.
- 18 M. Yoshida, T. Iizuka, Y. Saito, M. Onga, R. Suzuki, Y. Zhang, Y. Iwasa and S. Shimizu, *Nano Lett.*, 2016, **16**, 2061–2065.



- 19 T. Wang, C. Liu, J. Xu, Z. Zhu, E. Liu, Y. Hu, C. Li and F. Jiang, *Nanotechnology*, 2016, **27**, 285703.
- 20 K. Hippalgaonkar, Y. Wang, Y. Ye, D. Y. Qiu, H. Zhu, Y. Wang, J. Moore, S. G. Louie and X. Zhang, *Phys. Rev. B*, 2017, **95**, 115407.
- 21 J. J. Bae, H. Y. Jeong, K. H. Han, J. Kim, H. Kim, M. S. Kim, B. H. Moon, S. C. Lim and Y. H. Lee, *Nanoscale*, 2017, **9**, 2541–2547.
- 22 X. Zhang, D. Sun, Y. Li, G.-H. Lee, X. Cui, D. Chenet, Y. You, T. F. Heinz and J. C. Hone, *ACS Appl. Mater. Interfaces*, 2015, **7**(46), 25923–25929.
- 23 R. Yan, J. R. Simpson, S. Bertolazzi, J. Brivio, M. Watson, X. Wu, A. Kis, T. Luo, A. R. Hight Walker and H. G. Xing, *ACS Nano*, 2014, **8**, 986–993.
- 24 S. Sahoo, A. P. S. Gaur, M. Ahmadi, M. J.-F. Guinel and R. S. Katiyar, *J. Phys. Chem. C*, 2013, **117**, 9042–9047.
- 25 A. Taube, J. Judek, A. Łapińska and M. Zdrojek, *ACS Appl. Mater. Interfaces*, 2015, **7**, 5061–5065.
- 26 W. Zhou, X. Zou, S. Najmaei, Z. Liu, Y. Shi, J. Kong, J. Lou, P. M. Ajayan, B. I. Yakobson and J.-C. Idrobo, *Nano Lett.*, 2013, **13**, 2615–2622.
- 27 J. Hong, Z. Hu, M. Probert, K. Li, D. Lv, X. Yang, L. Gu, N. Mao, Q. Feng, L. Xie, J. Zhang, D. Wu, Z. Zhang, C. Jin, W. Ji, X. Zhang, J. Yuan and Z. Zhang, *Nat. Commun.*, 2015, **6**, 6293.
- 28 R. Addou, S. McDonnell, D. Barrera, Z. Guo, A. Azcatl, J. Wang, H. Zhu, C. L. Hinkle, M. Quevedo-Lopez, H. N. Alshareef, L. Colombo, J. W. P. Hsu and R. M. Wallace, *ACS Nano*, 2015, **9**, 9124–9133.
- 29 B. Stampfer, F. Zhang, Y. Y. Illarionov, T. Knobloch, P. Wu, M. Walzl, A. Grill, J. Appenzeller and T. Grasser, *ACS Nano*, 2018, **12**, 5368–5375.
- 30 Y. Chen, S. Huang, X. Ji, K. Adepalli, K. Yin, X. Ling, X. Wang, J. Xue, M. Dresselhaus, J. Kong and B. Yildiz, *ACS Nano*, 2018, **12**, 2569–2579.
- 31 H. Zuyun, Z. Ran, C. Xiaofei, C. Huijun, Z. Yunmin, S. Huimin, H. Shengxi, X. Jianming, D. Junfeng, C. Shuang, L. Meilin, W. Xinwei and Y. Chen, *ACS Appl. Mater. Interfaces*, 2018, **10**, 42524–42533.
- 32 D. Saha and S. Mahapatra, *J. Appl. Phys.*, 2016, **119**, 134304.
- 33 Y. Wang, K. Zhang and G. Xie, *Appl. Surf. Sci.*, 2016, **360**, 107–112.
- 34 B. Peng, Z. Ning, H. Zhang, H. Shao, Y. Xu, G. Ni and H. Zhu, *J. Phys. Chem. C*, 2016, **120**, 29324–29331.
- 35 Z. Ding, Q.-X. Pei, J.-W. Jiang and Y.-W. Zhang, *J. Phys. Chem. C*, 2015, **119**, 16358–16365.
- 36 M. Sharma, A. Kumar and P. Ahluwalia, *Phys. E*, 2019, **107**, 117–123.
- 37 J. M. Soler, E. Artacho, J. D. Gale, A. García, J. Junquera, P. Ordejón and D. Sánchez-Portal, *J. Phys.: Condens. Matter*, 2002, **14**, 2745–2779.
- 38 J. P. Perdew, K. Burke and M. Ernzerhof, *Phys. Rev. Lett.*, 1996, **77**, 3865–3868.
- 39 N. Troullier and J. L. Martins, *Phys. Rev. B: Condens. Matter Mater. Phys.*, 1991, **43**, 1993–2006.
- 40 S. Datta, *Electronic transport in mesoscopic systems*, Cambridge University Press, Cambridge, UK, 1995.
- 41 M. Brandbyge, J.-L. Mozos, P. Ordejón, J. Taylor and K. Stokbro, *Phys. Rev. B: Condens. Matter Mater. Phys.*, 2002, **65**, 165401.
- 42 W. Zhang, T. S. Fisher and N. Mingo, The atomistic green's function method: An efficient simulation approach for nanoscale phonon transport, *Numer. Heat Transfer, Part B*, 2007, **51**(4), 333–349.
- 43 C. Jeong, R. Kim, M. Luisier, S. Datta and M. Lundstrom, *J. Appl. Phys.*, 2010, **107**, 023707.
- 44 A. Naidu Gandhi and U. Schwingenschlögl, *EPL*, 2016, **113**, 36002.
- 45 X. Meng, T. Pandey, J. Jeong, S. Fu, J. Yang, K. Chen, A. Singh, F. He, X. Xu, J. Zhou, W.-P. Hsieh, A. K. Singh, J.-F. Lin and Y. Wang, *Phys. Rev. Lett.*, 2019, **122**, 155901.
- 46 C. Adessi, S. Roche and X. Blase, *Phys. Rev. B: Condens. Matter Mater. Phys.*, 2006, **73**, 125414.
- 47 B. Peng, H. Zhang, H. Shao, Y. Xu, X. Zhang and H. Zhu, *RSC Adv.*, 2016, **6**, 5767–5773.
- 48 D. L. Nika and A. A. Balandin, *J. Phys.: Condens. Matter*, 2012, **24**, 233203.
- 49 A. V. Krivosheeva, V. L. Shaposhnikov, V. E. Borisenko, J.-L. Lazzari, C. Waileong, J. Gusakova and B. K. Tay, *J. Semicond.*, 2015, **36**, 122002.
- 50 S. Ghatak, A. N. Pal and A. Ghosh, *ACS Nano*, 2011, **5**, 7707–7712.
- 51 H. Qiu, T. Xu, Z. Wang, W. Ren, H. Nan, Z. Ni, Q. Chen, S. Yuan, F. Miao, F. Song, G. Long, Y. Shi, L. Sun, J. Wang and X. Wang, *Nat. Commun.*, 2013, **4**, 2642.
- 52 P. Vancsó, G. Z. Magda, J. Pető, J.-Y. Noh, Y.-S. Kim, C. Hwang, L. P. Biró and L. Tapasztó, *Sci. Rep.*, 2016, **6**, 29726.
- 53 E. S. Kadantsev and P. Hawrylak, *Solid State Commun.*, 2012, **152**, 909–913.
- 54 W.-X. Zhou and K.-Q. Chen, *Sci. Rep.*, 2015, **5**, 15070.
- 55 W. Li, J. Carrete and N. Mingo, *Appl. Phys. Lett.*, 2013, **103**, 253103.
- 56 E. Abrahams, P. W. Anderson, D. C. Licciardello and T. V. Ramakrishnan, *Phys. Rev. Lett.*, 1979, **42**, 673–676.
- 57 G. P. Srivastava, *The Physics Of Phonons*, CRC Press, New York, 1990.
- 58 A. Togo and I. Tanaka, *Scr. Mater.*, 2015, **108**, 1–5.

